Plasma Phys. Control. Fusion **53** (2011) 105001 (18pp) doi:10.1088/0741-3335/53/10/105001

High spatial sampling global mode structure measurements via multichannel reflectometry in NSTX

N A Crocker[1], W A Peebles[1], S Kubota[1], J Zhang[1], R E Bell[2], E D Fredrickson[2], N N Gorelenkov[2], B P LeBlanc[2], J E Menard[2], M Podestà[2], S A Sabbagh[3], K Tritz[4] and H Yuh[5]

[1] Department of Physics and Astronomy, University of California–Los Angeles, Los Angeles, CA 90095-7099, USA
[2] Princeton Plasma Physics Laboratory, PO Box 451, Princeton, NJ 08543-0451, USA
[3] Department of Applied Physics and Applied Mathematics, Columbia University, New York, NY 10027, USA
[4] The Johns Hopkins University, Baltimore, MD 21218, USA
[5] Nova Photonics, Princeton, NJ 08540, USA

Received 12 March 2011, in final form 24 June 2011
Published 25 August 2011
Online at stacks.iop.org/PPCF/53/105001

Abstract

Global modes—including kinks and tearing modes ($f <\sim 50$ kHz), toroidicity-induced Alfvén eigenmodes (TAE; $f \sim$ 50–250 kHz) and global and compressional Alfvén eigenmodes (GAE and CAE; $f >\sim 400$ kHz)—play critical roles in many aspects of plasma performance. Their investigation on NSTX is aided by an array of fixed-frequency quadrature reflectometers used to determine their radial density perturbation structure. The array has been recently upgraded to 16 channels spanning 30–75 GHz ($n_{\mathrm{cutoff}} = (1.1\text{–}6.9) \times 10^{19}\,\mathrm{m}^{-3}$ in O-mode), improving spatial sampling and access to the core of H-mode plasmas. The upgrade has yielded significant new results that advance the understanding of global modes in NSTX. The GAE and CAE structures have been measured for the first time in the core of an NSTX high-power (6 MW) beam-heated H-mode plasma. The CAE structure is strongly core-localized, which has important implications for electron thermal transport. The TAE structure has been measured with greatly improved spatial sampling, and measurements of the TAE phase, the first in NSTX, show strong radial variation near the midplane, indicating radial propagation caused by non-ideal MHD effects. Finally, the tearing mode structure measurements provide unambiguous evidence of coupling to an external kink.

(Some figures in this article are in colour only in the electronic version)

1. Introduction

Toroidal fusion research plasmas exhibit a variety of global coherent perturbations that play critical roles in many aspects of plasma performance. For instance, kinks and tearing modes modify profiles and can cause transport (see [1] and references therein). Plasmas with energetic-ion populations created by neutral beam or radio frequency heating also commonly feature various fast-ion driven modes, including Alfvén eigenmodes and energetic particle modes (EPMs). Fast-ion modes cause redistribution or loss of the energetic ions, thereby changing the plasma energy and momentum sources, as well as potentially damaging plasma-facing components (see [2, 3], and references therein). High frequency Alfvén eigenmodes also potentially play a role in electron thermal transport [4].

The National Spherical Torus Experiment (NSTX) [5] features a rich spectrum of global modes. It exhibits tearing modes and kinks at $f <\sim 50$ kHz [6–10]. A wide variety of energetic-ion driven modes also exist in NSTX [11–17], including *beta-induced Alfvén-acoustic eigenmodes* (BAAE) [16–18] and EPM [13, 14, 19–21] at $f <\sim 50$ kHz, *reversed shear* (RSAE) [15, 22, 23] and *toroidicity-induced* (TAE) [14, 24–26] Alfvén eigenmodes in the range $f \sim 50$–250 kHz, and *global* (GAE) [12, 14, 27, 28] and *compressional* (CAE) [11, 12, 14, 29–32] Alfvén eigenmodes at $f >\sim 400$ kHz. Figure 1 shows a magnetic fluctuation spectrum illustrating the broad variety of modes in a typical NSTX beam-heated plasma. (Note that the frequencies at which the modes are observed are significantly Doppler shifted by toroidal rotation. Toroidal rotation frequencies, as measured by charge exchange recombination spectroscopy (CHERS) [33], can typically be up to $f_{\mathrm{ROT}} \sim 50$ kHz and the toroidal mode numbers of the various mode described above can be up to $|n| \sim 10$.)

The investigation of global modes and their impact on the NSTX plasma is facilitated by an array of fixed-frequency quadrature reflectometers that is routinely utilized to investigate the spatial structure of their associated density perturbations [14, 15, 34–40]. The array was recently upgraded to 16 channels, thereby significantly improving spatial sampling and the resolution of mode structure measurements. The upgraded array operates over a frequency range from 30 to 75 GHz, with equivalent O-mode cutoff densities ranging from 1.1×10^{19} to 6.9×10^{19} m^{-3}, thereby significantly increasing the upper limit of accessible density and allowing access to the core of high performance, beam-heated H-mode plasmas in NSTX. The full array consists of two distinct 8-channel systems with frequencies in the ranges 30–50 GHz and 55–75 GHz, respectively. Each system uses a microwave circuit very similar to one employed successfully by Peebles *et al* to implement an eight-frequency array of Doppler reflectometers in the DIII-D tokamak [41].

The unique capabilities of the array have been exploited to obtain significant new measurements of several types of global modes, including GAEs and CAEs, TAEs and tearing modes. The GAE and CAE structures have been measured for the first time in the core of an NSTX high-power (6 MW) beam-heated H-mode plasma. GAEs are of interest because enhanced electron thermal transport in the core of NSTX beam-heated has recently been observed to correlate with GAE activity [4]. Their role in electron thermal transport is currently under active investigation [4, 42–44] and the new structure measurements are critical to improved understanding of their role [44]. The CAE structure measurements demonstrate that they are strongly core-localized, suggesting they may also be candidates for explaining the enhanced core electron thermal transport for similar reasons as GAEs. New TAE structure measurements have been obtained with a significantly increased spatial sampling compared with previous measurements in NSTX [37–39]. In addition, the measurements include not just TAE amplitude, but also phase, a first in NSTX. A strong radial variation of phase is observed, indicating radial propagation caused by non-ideal MHD effects, a topic of emerging interest

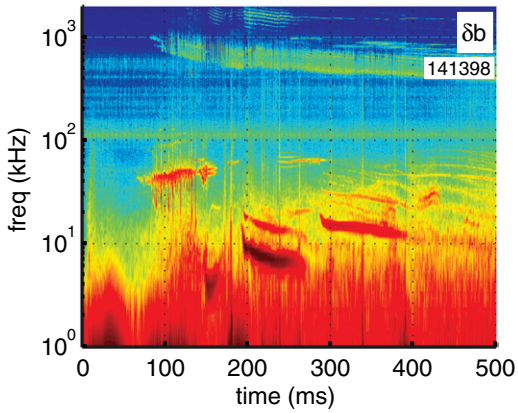

Figure 1. The magnetic fluctuation spectrum for NSTX beam-heated plasma (shot 141398).

in the experimental investigation of fast-ion modes in tokamaks [45–47]. Finally, the tearing mode structure has been measured, providing unambiguous evidence of coupling between tearing modes and external kinks. Coupling of tearing modes to kinks is actively investigated in NSTX [6, 8–10] and other tokamaks [48–51], but little attention has been given to the edge structure of the coupled kink-tearing modes. These results motivate the need for such attention in future investigations of coupled kink-tearing modes.

The rest of this paper discusses these issues in greater detail. Section 2 provides an overview of the technical aspects of the upgraded reflectometer array and summarizes the new measurement capabilities. Section 3 presents the mode structure measurements for each type of mode with a discussion of some of the implications. In particular, sections 3.1, 3.2 and 3.3 treat, respectively, the structure measurements of GAEs and CAEs, TAEs and tearing modes. The paper concludes with a summary in section 4.

2. Upgraded reflectometer array

The upgraded reflectometer array consists of two eight-channel systems with frequencies in the ranges 30–50 GHz and 55–75 GHz. Each system utilizes a single microwave circuit to generate all the launch frequencies, which are coupled to and received from the plasma using a pair of closely spaced horns (i.e. directional antennas). The two systems are referred to here as *Q-band* and *V-band*, respectively, based on the microwave frequency bands utilized. The frequencies of the Q-band system are coupled to the plasma using a Q-band waveguide, whose normal frequency range is the 33–50 GHz. However, the Q-band waveguide transmits down to frequencies as low as the cutoff frequency of ∼26.4 GHz and so operation to 30 GHz suffers little loss. The frequencies of the V-band system all fall within the 50–75 GHz nominal transmission band of the V-band waveguide, which is used in coupling the system to the plasma. As illustrated in figure 2, the two horn pairs are separated 10.2° toroidally from each other (figure 2(*b*)) and positioned at approximately the same vertical location, ∼13 cm above the midplane at $R = 171$ cm (figure 2(*a*)). The horns are oriented to launch and receive approximately normal to the NSTX flux surfaces (figure 2(*a*)) so that using the same pair of horns for multiple frequencies produces a radially distributed array of measurements. Each system can be configured to launch microwaves with either O- or X-mode polarization. The horns are circular and coupled to the rectangular waveguide via an assembly including a rotary

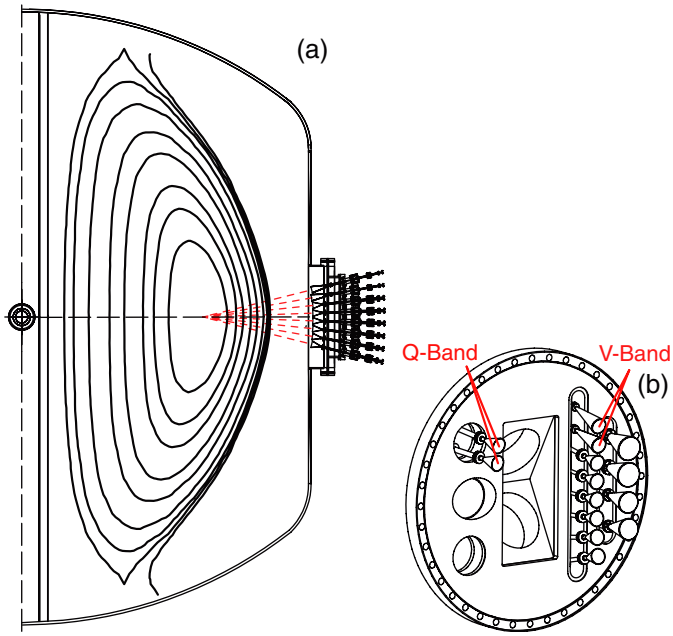

Figure 2. (*a*) Cross-section of the NSTX vacuum vessel with typical plasma flux surfaces at the location of the vertical array containing V-band antennas; (*b*) interior view of the vacuum vessel port flange showing the Q-band (30–50 GHz) and V-band (55–75 GHz) antennas.

joint and a rectangular–circular transition. The rotary joint allows the antenna polarizations to be easily selected (e.g. O or X-mode).

The microwave circuits utilized in the two systems are very similar to one employed successfully by Peebles *et al* to implement an eight-frequency array of Doppler reflectometers in the DIII-D tokamak [41]. The circuit is illustrated schematically in figure 3, neglecting amplifiers and attenuators used to manage power levels. As can be seen, the heart of the microwave circuit is a nonlinear transmission line (NTL). The NTL generates a broad array of harmonics from a stable, low phase noise, 2.5 GHz microwave source. Bandpass filters are then used to select frequency subsets. In the Q-band circuit, harmonics in the 30–50 GHz range are selected, whereas in the V-band circuit, harmonics in the 27.5–37.5 GHz range are selected and doubled in frequency. (It should be noted that the doubler not only doubles the input frequencies to generate 55, 60, 65, 70 and 75 GHz, but, through internal mixing or intermodulation, also generates equally strong frequency components at adjacent intermediate frequencies. This results in output frequencies ranging from 55 to 75 GHz in 2.5 GHz increments.) A coupler splits the resulting microwave power into two portions, a *signal* and *reference*, each of which contains all the frequencies of the subset. A pair of closely spaced horns is utilized to launch the *signal* power into the plasma and capture the reflection from the plasma. Both the *reference* and the reflected *signal* are downshifted in frequency to an intermediate range of 0.5–10.5 GHz by mixing with a separate, stable microwave source. In the Q-band circuit, the frequency of this source is 40.5 GHz, while in the V-band circuit it is 64.5 GHz. An eight-way power splitter and a set of narrow-band (150 MHz) bandpass filters are then used to isolate the individual intermediate frequencies. The selected frequencies are 2, 3, 4.5, 5.5, 7, 8, 9.5 and 10.5 GHz. For the Q-band circuit, these uniquely correspond to launch frequencies of 42.5, 37.5, 45, 35, 47.5 32.5, 50 and 30 GHz. For the V-band circuit, they uniquely correspond to 62.5, 67.5,

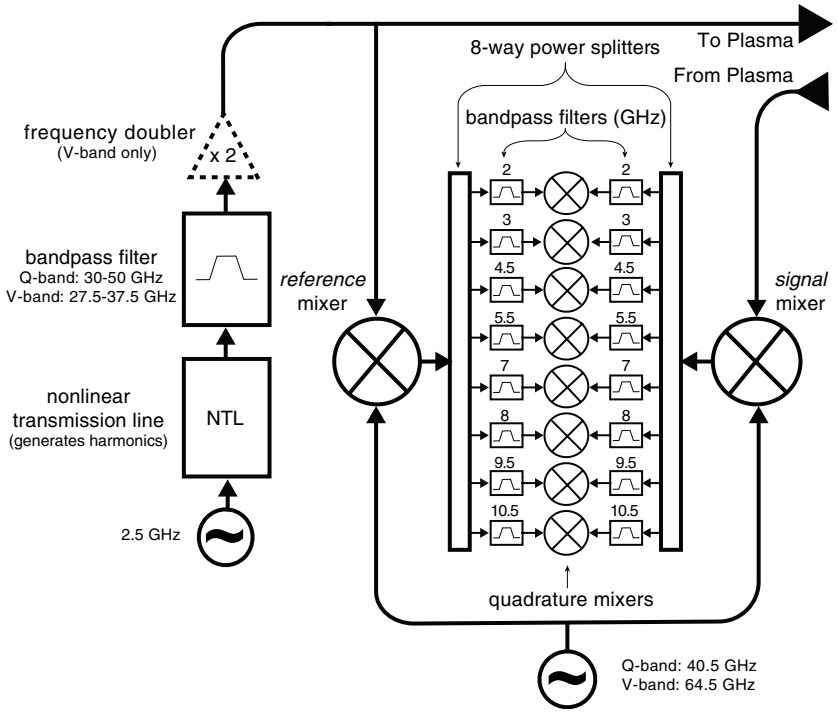

Figure 3. Schematic of the 8-frequency microwave circuit. (Amplifiers, attenuators and other power management circuit elements not shown.)

60, 70, 57.5, 72.5, 55 and 75 GHz. (Note that this results in an array of frequencies for the combined systems ranging from 30 to 75 GHz in 2.5 GHz increments, excluding 40, 52.5 and 65 GHz.) At each of the filtered intermediate frequencies, a quadrature mixer utilizes the downshifted *signal* and *reference* to obtain the in-phase (I) and quadrature (Q) electric field components of the *signal*.

Global modes in the plasma cause the optical path length to fluctuate for each of the frequencies in the *signal*. Since each frequency reflects at a different location, the array of path length fluctuations gives a measurement of the mode structure. The path length fluctuation for each frequency can be determined by the values of I and Q measured for that frequency. Specifically, the path length fluctuation is given by $\delta\Phi/k_0$, where k_0 is the vacuum wavenumber and $\delta\Phi$ is the fluctuating phase of the complex electric field $E \equiv I + \mathrm{i}Q = A\exp(\mathrm{i}\delta\Phi)$. The path length fluctuation due to a particular mode is obtained by filtering $\delta\Phi$ to isolate a narrow band around the mode frequency. Also, in keeping with the global nature of the mode, the result may be further refined by isolating the component that is coherent with a suitable reference signal. For the results presented here, edge magnetic coil signals that have been similarly bandpass filtered are used. The resulting $\delta\Phi$ for each reflectometer channel is characterized by an amplitude and a temporal phase, and may expressed as a complex number. The component of $\delta\Phi$ that is incoherent with the reference signal, $\delta\Phi_{\mathrm{incoh}}$, represents a source of statistical uncertainty, $[\langle|\delta\Phi_{\mathrm{incoh}}|^2\rangle/N]^{1/2}$, where $N =$ (filter bandwidth)$\times$(record length) represents the number of independent statistical measurements. For the analysis here, the reflectometer signals are sampled at 10 MHz and the magnetic coil signals are sampled at 4 MHz. The analysis bandwidth and record lengths used for each mode are indicated in the

presentation of measurements below. The structure measured for each mode can be expressed in terms of the variation with cutoff radius of the *effective radial displacement*, ξ, defined as half the path length fluctuation (i.e. $\xi \equiv \delta\Phi/2k_0$). Effective radial displacement is a good approximation of the cutoff surface displacement for global coherent density perturbations with large radial extent [52]. For perturbations with shorter radial extent, the details of the perturbation radial structure along the path become important, but ξ is still most sensitive to the density perturbation near cutoff [52]. In this case, the effective displacement is useful for an initial estimate of the structure but modeling of the microwave propagation will yield an improved interpretation of the measurements. (See, for example, [52] for a discussion of issues related to the interpretation of reflectometer measurements. See also [36, 38, 40] for examples of more sophisticated interpretation techniques applied to NSTX research.) The relationship between cutoff displacement and the actual plasma displacement depends, of course, on the details of the mode, such as whether it shears or compresses the plasma.

Although both sub-arrays can be configured to launch either O- or X-mode polarized microwaves, the upgraded array is typically configured for O-mode. In NSTX, the on-axis toroidal magnetic field typically ranges from 3.5 to 5.5 kG, while plasma densities can reach $\sim 10^{20}\,\mathrm{m}^{-3}$. For such plasma conditions, the locations of the cutoff for O- and X-mode typically differ insufficiently for the choice of polarization to offer any significant advantage in terms of plasma accessibility. The choice of polarization in NSTX is instead influenced by the relative ease of determining cutoff locations for O-mode compared with X-mode. For both polarizations, determination of the cutoff location requires knowledge of the plasma density profile, which is reliably obtained in NSTX via multi-point Thomson scattering (MPTS) [53]. For, X-mode, however, knowledge of the magnetic field structure is also required. In order to obtain this information with sufficient accuracy, equilibrium reconstruction constrained by a motional Stark effect (MSE) [54] measurement of the magnetic field pitch angle is essential. Since MSE data are not currently available for all plasma conditions in NSTX, O-mode polarization is almost exclusively employed.

The upgrade extends the range of accessible densities up to $6.9 \times 10^{19}\,\mathrm{m}^{-3}$, substantially improving access to the core of high-power (up to 6 MW) beam-heated H-mode plasmas in NSTX. In such plasmas, peaks in the edge density with values $>\sim 4 \times 10^{19}\,\mathrm{m}^{-3}$ commonly develop quickly as the plasma enters H-mode, increasing even further to $\sim 5 \times 10^{19}\,\mathrm{m}^{-3}$ as the density profile evolves from hollow to centrally peaked. Figure 4 shows a typical example (shot 141398). Time histories of key plasma parameters for this example are shown in figure 4(*a*). The plasma enters H-mode in the early period of 6 MW beam injection. Figure 4(*b*) shows the evolution of the density profile as measured by MPTS.

The increased number of reflectometer channels significantly improves spatial sampling and the resolution of mode structure measurements. Figure 5(*a*) shows an example of the radial coverage and spatial sampling attainable in high-power beam-heated H-mode plasmas (shot 141398 at $t = 582$ ms). Notably, twelve of the reflectometers have frequencies in the range 30–62.5 GHz, providing access to plasmas with densities in the range $n_{\mathrm{cutoff}} = (1.1\text{–}4.8) \times 10^{19}\,\mathrm{m}^{-3}$. This represents a significant increase in spatial sampling even within the range of densities accessible prior to the upgrade. Figure 5(*b*) shows an example of the coverage and spatial sampling attainable in an L-mode plasma (shot 141707 at $t = 448$ ms) of the type typically created for the study of TAEs in NSTX [37–39]. (Note that the density profiles shown in figure 5 are smoothed, which has a small effect on the determination of the cutoff radii. Also the profiles in figures 5(*a*) and (*b*) are scaled by factors of 1.085 and 1.08, respectively, to ensure consistency between the MPTS and reflectometer measurements. The evolution of the peak density measured by MPTS can be used to accurately predict the periods during which the microwaves of each channel reflect from the plasma when scaled by the indicated factors.

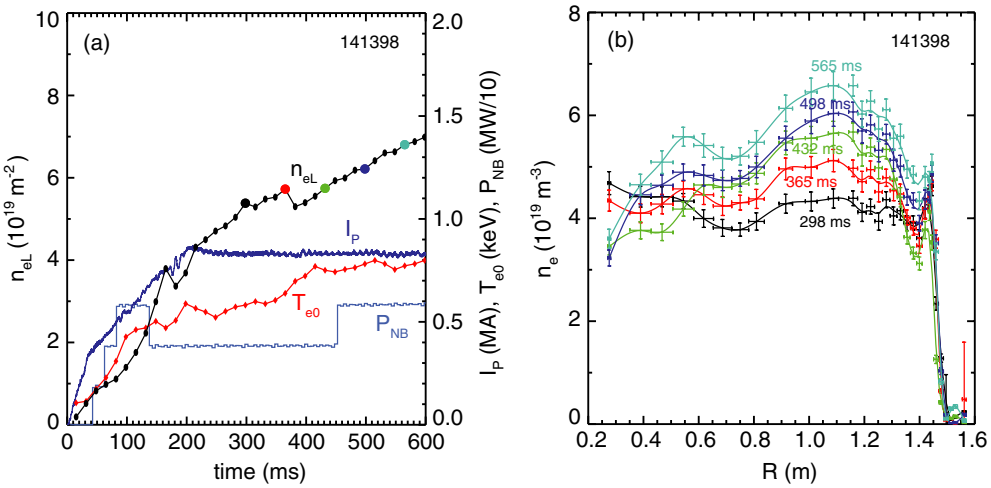

Figure 4. (*a*) Time history of plasma current (I_P), neutral beam power (P_{NB}), and central electron temperature (T_{e0}) and line average density (n_{eL}) from MPTS; (*b*) electron density profiles from MPTS for the times indicated by solid circles (●) in figure 4(*a*). Crosses indicate measurements with error bars. Lines show smoothed profiles.

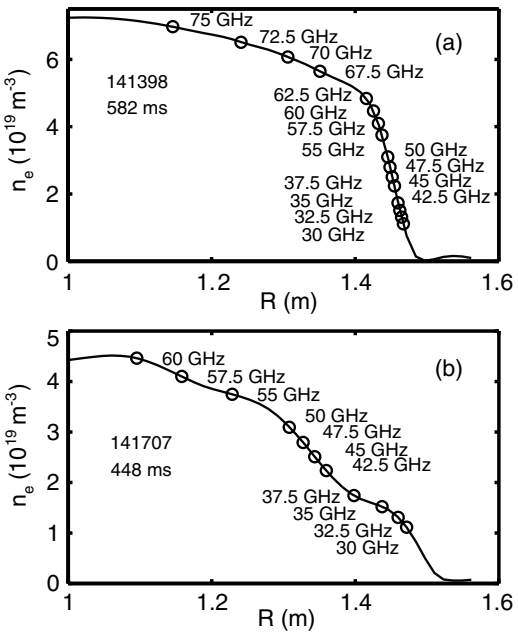

Figure 5. NSTX density profiles from (smoothed) MPTS for (*a*) high-power (4 MW) beam-heated H-mode plasma and (*b*) high density L-mode plasma. O-mode cutoff locations indicated for frequencies of the upgraded reflectometer array.

When peak plasma density exceeds the critical value for a channel, reflection from the plasma starts and the level of reflected power detected increases sharply and substantially ($>\sim$10 dB in $<\sim$10 ms). A corresponding decrease in the power level is observed when reflection ends. This consistency requirement strongly constrains the determination of the scaling factor. The

MPTS density measurements are normally compensated for by a plasma-induced coating on the MPTS observation window with a scaling factor periodically determined by comparison with line integrated density from the FIReTIP far infrared tangential interferometers [55]. For figures 5(*a*) and (*b*), those scalings, 1.58 and 1.72, were determined in each case from measurements obtained several days earlier. The reflectometer-based scalings compensate for the additional coating. Comparisons of MPTS with FIReTIP in the same shots as figures 5(*a*) and (*b*) confirm the need for the additional scaling factors.)

3. Mode structure measurements

The capabilities of the upgraded array have been exploited to obtain new structure measurements of several types of global modes. These results include structure measurements of GAEs and CAEs, discussed in section 3.1, TAEs, discussed in section 3.2, and tearing modes, discussed in section 3.3.

3.1. Global and compressional Alfvén eigenmodes

GAEs and CAEs are commonly observed in beam-heated NSTX plasmas [11, 12, 14]. The increased range of densities accessible by the upgraded reflectometer array enables, for the first time, the investigation of the GAE and CAE structure in the core of high-power beam-heated H-mode plasmas in NSTX. Figure 6 shows the first such measurements. Figure 6(*a*) shows a spectrum of coherent modes in the 350–900 kHz frequency range observed by edge magnetic coils in a high-power (6 MW) beam-heated H-mode plasma (shot 141398). (Time histories of key plasma parameters for this shot are shown in figure 4(*a*).) Figure 6(*b*) shows an expanded view of the same magnetic spectrum around $t = 580$ ms, which is shortly after all channels of the array have begun to reflect. Figure 6(*c*) shows the spectrum of phase fluctuations from a core reflectometer (72.5 GHz). Many of the same modes visible in the magnetic spectrum are also visible in the reflectometer spectrum, indicating their global nature. Structure measurements for several of the strongest modes (i.e. strongest as measured by the core reflectometers), at frequencies of $f = 401$, 633, 648 and 726 kHz, are shown in figure 6(*d*). (Figure 5(*a*) shows the density profile and reflectometer cutoff locations for the time period in figures 6(*b*) and (*c*).) The amplitude of the effective radial displacement, $|\xi|$, is plotted versus cutoff radius. For the modes shown in figure 6(*d*), the bandwidths used for the analysis range from 6 to 9 kHz and were chosen based on the observed spectral bandwidth of the mode. Measurements of mode phase versus toroidal angle, obtained using 10 magnetic sensing coils from a toroidally distributed edge array, yield toroidal mode numbers of $n = -8, -4, -3$ and -3, respectively, for the $f = 401, 633, 648$ and 726 kHz modes. The modes propagate counter to the direction of neutral beam injection, which is indicated by the negative sign of the toroidal mode numbers. Structure measurements (not shown) at $t = 580$ ms of many of the other modes visible in figures 6(*b*) and (*c*) indicate that the modes can be divided into two groups. Modes with frequencies $f >\sim 500$ kHz have strongly core-localized structures like those of the $f = 633$, 648 and 726 kHz modes in figure 6(*d*), which are the strongest of the group. In contrast, modes with frequencies $f <\sim 500$ kHz have structures, similar to that of the $f = 401$ kHz mode in figure 6(*d*), that peak toward the magnetic axis, but have very broad radial extent. The $f = 401$ kHz mode is the strongest of this group.

The frequencies and propagation direction of the modes shown in figure 6(*d*) indicate that they are either GAEs or CAEs excited by Doppler shifted cyclotron resonance with the beam ions [12], which are commonly observed in NSTX beam-heated plasmas. The plasma ion species is deuterium, and, at the time of measurement ($t = 580$ ms), the

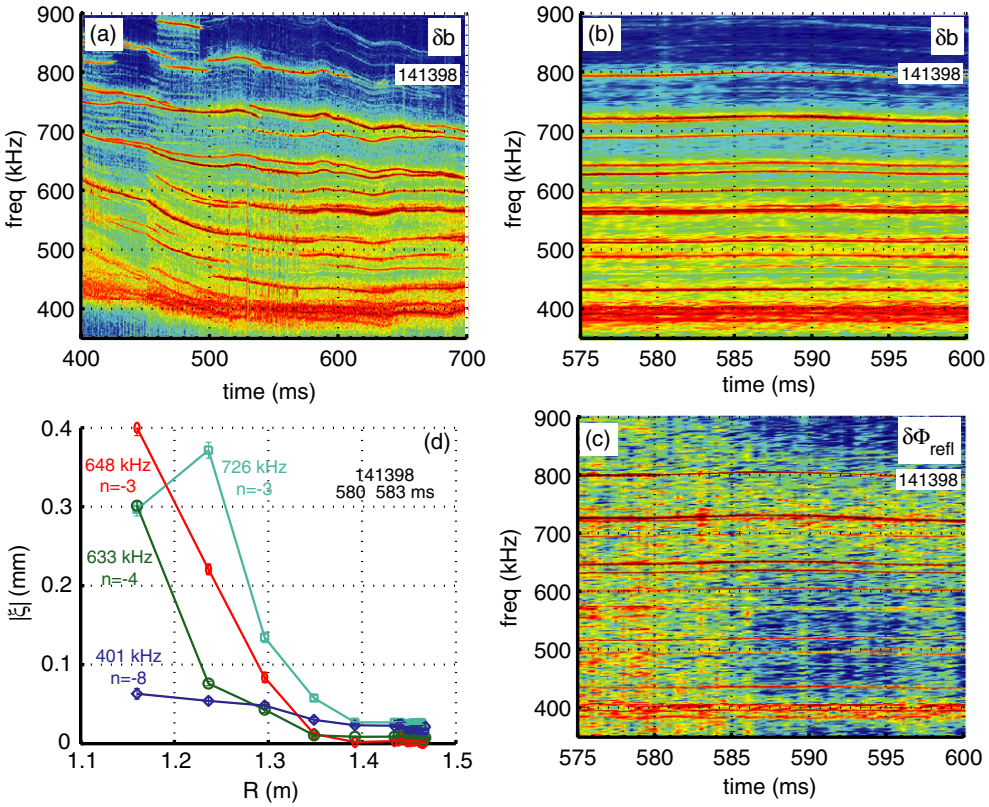

Figure 6. (*a*) Spectrum of magnetic fluctuations (shot 141398) showing multiple high frequency modes identified as GAEs ($f <\sim 500$ kHz at $t = 580$ ms) and CAEs ($f >\sim 500$ kHz at $t = 580$ ms); (*b*) expanded view of magnetic fluctuations shortly after all reflectometers have begun to reflect; (*c*) core reflectometer (72.5 GHz at $R \sim 1.24$ m) phase fluctuations during the same period; (*d*) radial structure of effective displacement amplitude for strongest CAEs ($f = 633$, 648 and 726 kHz) and strongest GAE ($f = 401$ kHz), with toroidal mode numbers indicated.

magnetic field and electron density at the magnetic axis ($R_0 \approx 1.05$ m) are 0.32 T and 7.2×10^{19} m^{-3}, giving an Alfvén velocity of $V_{A0} = 5.8 \times 10^5$ m s^{-1} and an Alfvén frequency of $f_{A0} = V_{A0}/2\pi R_0 \approx 89$ kHz. The beams inject 6 MW of neutral beam power using 90 keV deuterons. The beam ion velocity is $V_B = 3 \times 10^6$ m s^{-1}, which is significantly faster than V_{A0}. The modes propagate counter to the beam injection direction and have frequencies significantly higher than f_{A0}, but below the ion cyclotron frequency, $f_{CD0} = eB_0/2\pi m_D = 2.4$ MHz. Propagation counter to the beam injection direction Doppler shifts the mode frequency higher in the beam ion frame, enabling the cyclotron resonance [12].

To distinguish the specific type of each mode in figure 6(*d*), GAE or CAE, the mode frequency evolution, visible in figure 6(*a*), can be compared with expectation. GAEs are shear Alfvén eigenmodes that peak in the region of the weak magnetic shear near the magnetic axis [12, 27] with frequencies $f_{GAE} \approx |k_\parallel| V_{A0}/2\pi + (n/R_0) f_{ROT0}$, where $k_\parallel \approx (m/q_0 - n)/R_0$ is the wavenumber parallel to the magnetic field and f_{ROT0} is the toroidal rotation frequency at the magnetic axis. CAEs are eigenmodes in a 'potential well' created by the region in the plasma where compressional Alfvén waves can propagate [11, 12, 35]. For compressional Alfvén waves with toroidal wave number n, the potential well is the region where $(\omega/V_A)^2 > (n/R)^2$. In addition to the toroidal mode number, the spectrum of CAEs can be characterized by

generalized poloidal and radial mode numbers, M and S. CAEs have frequencies given by $f_{\rm CAE} \approx (V_{\rm A}/2\pi)[n^2/R^2 + \delta^2]^{1/2} + (n/R) f_{\rm ROT}$, where $V_{\rm A}$, $f_{\rm ROT}$ and R are evaluated where the mode is localized, at the maximum of $(\omega/V_{\rm A})^2 - (n/R)^2$, and δ^2 depends on the poloidal and radial structure of the modes. For a given n, the value of δ^2 is determined by M and S. Lower values of M and S correspond, in general, to mode structures with larger poloidal and radial scales. For high values of M and S, it is illustrative to think of δ^2 as $\delta^2 \approx k_\theta^2 + k_r^2 = M^2/r^2 + S^2/L_r^2$, where r is the minor radius of mode localization and L_r is the radial scale of the potential well.

The expected frequencies for GAEs and CAEs are both sensitive to toroidal rotation and the Alfvén frequency, but in different ways. In addition, GAEs are sensitive to the plasma safety factor, q, at the magnetic axis. CHERS measurements indicate that the toroidal rotation frequency at the magnetic axis is $f_{\rm ROT0} \approx 23$ kHz (in the beam injection direction) from $t = 400$ ms to $t = 550$ ms, trending downward afterwards to $f_{\rm ROT0} \approx 15$ kHz at $t = 700$ ms. Equilibrium reconstruction with the LRDFIT code [7, 56, 57]—constrained by edge magnetic measurements and MSE field pitch measurements—is used to determine the safety factor, q. The safety factor at the magnetic axis, which is determined within $\pm\sim$0.1, trends downward from $q_0 \approx 1.7$ at $t = 400$ ms to $q_0 \approx 1.1$ at $t = 700$ ms. Taking into account the ion species, the electron density from MPTS and the magnetic field on axis from LRDFIT, $f_{\rm A0}$ trends downward from $f_{\rm A0} \approx 110$ kHz at $t = 400$ ms to $f_{\rm A0} \approx 82$ kHz at $t = 700$ ms. (Note that the assumption that mass density is given by $m_{\rm D} n_{\rm e0}$ affects the determination of $f_{\rm A0}$. It gives the correct value if significant impurities have the same charge-to-mass ratio as deuterium, which is likely to be the case since the most significant impurity is carbon.) At the time of the mode structure measurements, $q_0 \approx 1.3$, $f_{\rm ROT0} \approx 22$ kHz and $f_{\rm A0} \approx 89$ kHz.

Comparison with expectations for GAE and CAE frequencies shows that the $f = 633$, 648 and 726 kHz modes are CAEs, while the $f = 401$ kHz mode is a GAE. The large toroidal mode number, $n = -8$, and low frequency of the $f = 401$ kHz mode are sufficient to identify it as a GAE. Taking into account the Doppler shift, a CAE with a toroidal mode number of $n = -8$ would be expected to have a frequency $f > 600$ kHz. However, the higher frequencies of the $f = 633$, 648 and 726 kHz modes, and their lower mode numbers, $n = -4$, -3 and -3, are not consistent with expectations for GAEs in light of the strong downward trend in q_0. In order to fit the dispersion relation for GAEs as well as possible at $t = 580$ ms, these modes need relatively large poloidal mode numbers of $m \approx 5$, 7 and 8, respectively. (This would give mode frequencies of ∼601, 667 and 734 kHz, respectively.) Consequently, the contribution of m/q_0 to each of their frequencies would make its evolution very sensitive to the trend in q_0, causing it to evolve inconsistently with observation. The observed frequencies of the $f = 633$ and 648 kHz modes (figure 6(*a*)), while evolving slightly differently over time, trend downward from $f \approx 700$ kHz to $f \approx 620$ kHz between $t \approx 400$ ms and $t \approx 700$ ms. In contrast, the frequencies of $(m, n) = (5, -4)$ and $(7, -3)$ GAEs would evolve distinctly differently. Initially, they would both decrease by $\Delta f >\sim 50$ kHz between $t = 400$ ms and $t \sim 570$ ms. Afterward, however, they would both increase until $t = 700$ ms, by $\Delta f >\sim 40$ kHz. Similarly, the observed frequency of the $f = 726$ kHz mode trends downward from $f \approx 740$ kHz to $f \approx 700$ kHz between $t \approx 530$ ms and $t \approx 680$ ms. In contrast, the frequency of an $(m, n) = (8, -3)$ GAE would be expected to increase by $\Delta f \sim 50$ kHz between $t \approx 530$ ms and $t \approx 680$ ms. The expectation for increasing frequencies is mostly due to the strong upward trend in m/q_0 resulting from the large expected poloidal mode numbers, m, and the strong downward trend in q_0. The decreasing Doppler shift also contributes. The downward trend in $f_{\rm A0}$ works against these factors, but is not strong enough to overcome them.

While not consistent with the expectation for GAEs, the frequency trends of the $f = 633$, 648 and 726 kHz modes are consistent with the expectation for CAEs, assuming values of δ

ranging from $\sim 1/(0.16\,\mathrm{m})$ to $\sim 1/(0.13\,\mathrm{m})$ that decrease slightly ($<\sim 10\%$) over time for each mode. The effective displacement of the modes is strongly core localized, largely confined to $(R–R_0) <\sim 30\,\mathrm{cm}$. This indicates that the modes have short radial scales, roughly consistent with such values for δ if the modes have low M (e.g. $|M| = 0, 1$). Comparison with detailed theoretical predictions for CAE frequency and structure, as well as modeling of the reflectometer response, would be necessary to determine the values of M and S for each of the modes. However, it is worth noting that the observed mode structures appear to be qualitatively consistent with low values of M. The measured structures of the $f = 633$ and 648 kHz modes indicate peaking very near the magnetic axis. This would be expected for CAEs with low n and $M = 0$, since CAEs with $M = 0$ will peak at the maximum of $(\omega/V_\mathrm{A})^2 - (n/R)^2$, which will be close to the axis for low n. The measured structure of the $f = 726$ kHz mode indicates peaking off, but still close to, the axis. This type of peaking would be expected for CAEs with low M, where $M \neq 0$.

The observed core-localized structure of the CAEs opens up the intriguing possibility that they may play a role in electron thermal transport. Enhanced electron thermal transport in the core of NSTX beam-heated H-mode plasmas has recently been observed to correlate with GAE activity [4]. The role of GAEs in the electron thermal transport is currently under investigation [4, 42–44]. One hypothesis holds that GAEs have frequencies permitting resonant interactions with electrons that can perturb their orbits, leading to electron thermal transport. Furthermore, since GAEs are expected to peak in the region of weak shear near the magnetic axis, they would be expected to have a significant effect in the core. The CAEs discussed here have similar frequencies to the GAEs, indicating they may also have the potential for wave–electron interactions that can lead to thermal transport. CAEs have been considered unlikely candidates for explaining the enhanced electron thermal transport because of an expectation that they would peak away from the plasma core [43]. Notably, the dominant CAEs ($f = 633$, 648 and 726 kHz in figure 6(*d*)) have significantly greater amplitude in the plasma core than the dominant GAE ($f = 401$ kHz in figure 6(*d*)). This indicates that while the observed GAEs may, in fact, contribute to the electron thermal transport as hypothesized, the CAEs need to also be considered since they may actually make a greater contribution. The results presented here motivate future theoretical modeling of CAE structures and their interactions with electrons in order to evaluate the contribution to core electron thermal transport.

3.2. Toroidicity-induced Alfvén eigenmodes

TAEs are frequently observed in beam-heated NSTX plasmas, where their investigation has been routinely facilitated by structure measurements via reflectometry [37–39]. The upgraded reflectometer array has enabled measurement of the TAE structure with substantially improved spatial sampling. Figure 7 shows the first such measurements. Figure 7 also shows the first measurements of TAE phase versus radius in NSTX, an aspect of mode structure that has received little attention in the experimental investigation of TAEs. Figure 7(*a*) shows a magnetic fluctuation spectrum from edge magnetic coils featuring coherent bursting and chirping modes with frequencies in the range $f = 50$–150 kHz (shot 141707). Figure 7(*b*) shows an expanded view of the same magnetic spectrum around $t = 447$ ms, which is shortly after the 60 GHz channel has begun to reflect. Figure 7(*c*) shows the 60 GHz reflectometer spectrum, which reflects in the core of the plasma. The modes visible in the magnetic spectrum are also visible in the reflectometer spectrum, indicating their global nature. The spatial structure of several of the modes, measured by the reflectometers during one of the bursts ($t = 447$ ms), is shown in figures 7(*d*) and (*e*). The frequencies of the modes are $f = 77$, 97 and 121 kHz. The bandwidths used for the analysis were 11, 19 and 17 kHz, respectively.

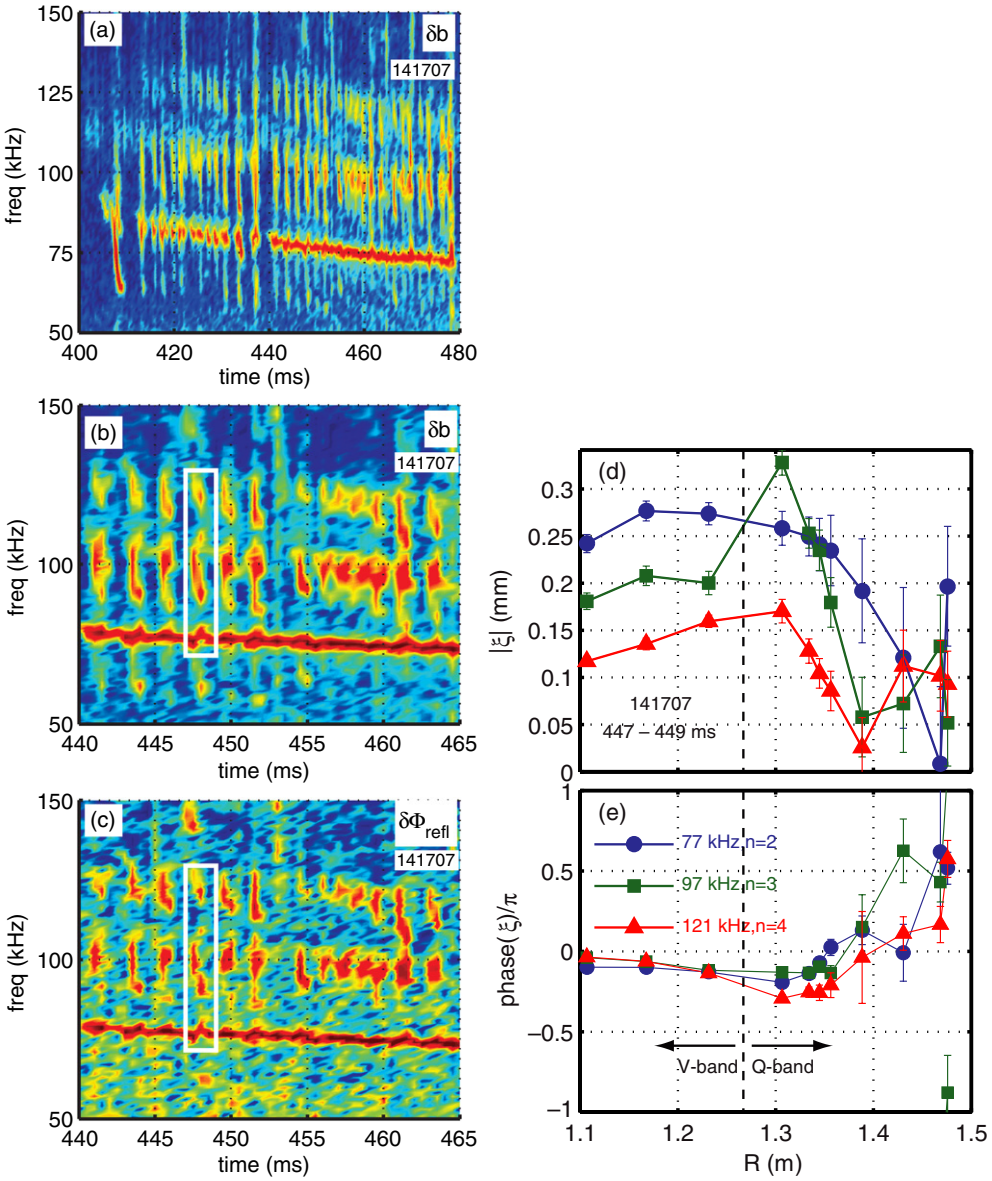

Figure 7. (*a*) Spectrum of magnetic fluctuations (shot 141707) showing modes identified as TAEs; (*b*) expanded view of magnetic fluctuations shortly after the 60 GHz reflectometer has begun to reflect; (*c*) core reflectometer (60 GHz at $R \sim 1.1$ m) phase fluctuations during the same period; radial structure of effective displacement (*d*) amplitude and (*e*) phase for highest amplitude TAEs during chirp at $t = 447$ ms. The legend shows mode frequency and toroidal mode number, n. Boxes in figures 7(*b*) and (*c*) highlight analyzed modes. Phase in figure 7(*e*) is corrected for toroidal separation between Q- and V-band antennas. Location of Q- and V-band reflectometers cutoffs indicated in figure 7(*e*).

(Figure 5(*b*) shows the density profile and reflectometer cutoff locations for the time period in figures 7(*b*) and (*c*).) Specifically, figures 7(*d*) and (*e*), respectively, show the amplitude ($|\xi|$) and phase (arctan[Im(ξ)/Re(ξ)]) of the effective radial displacement versus cutoff radius. The sign convention for the phase is that the decreasing phase implies increasing temporal

delay. Consequently, the increase of phase with radius apparent in figure 7(*e*) for $R >\sim 1.3$ m indicates that the response of the core reflectometers to the mode is delayed relative to the response of the edge reflectometers. Toroidal mode numbers were determined for the modes using 10 magnetic sensing coils in an array toroidally distributed around the edge of NSTX. The mode numbers are $n = +2, +3$ and $+4$, respectively, for the $f = 77$, 97 and 121 kHz modes. The modes propagate in the direction of beam injection, which is indicated by the positive sign of the mode numbers. The phase shown in figure 7(*e*) is corrected for a shift due to the small difference in the Q- and V-band toroidal locations. (The figure indicates which measurements are Q-band and V-band.) A correction of $n\pi(10.2^\circ/180^\circ)$ radians was subtracted from the phase measured by the V-band reflectometers for each mode.

The modes in figure 7 are identified as TAEs based, in part, on their bursting and chirping character. The plasma is heated with 2 MW of neutral beam power using a 90 keV deuterium beam. The beam ion velocity is $V_B = 3 \times 10^6\,\mathrm{m\,s^{-1}}$. The magnetic field at the magnetic axis ($R_0 \approx 1.05$ m) is 0.5 T, the ion species is deuterium and the peak electron density from MPTS is $n_{e0} = 4.5 \times 10^{19}\,\mathrm{m^{-3}}$, giving an Alfvén velocity of $V_{A0} = 1.15 \times 10^6\,\mathrm{m\,s^{-1}}$. The beam ion velocity is significantly faster than V_{A0}, enabling the excitation of TAEs by beam ions. The $n = 3$ and 4 modes both exhibit bursts featuring rapid ($\Delta t <\sim 1$ ms) substantial downward frequency chirps ($|\Delta f/f| \sim 10\%$ kHz) over the period shown in figure 7(*a*). This is a characteristic commonly exhibited by TAEs due to their interaction with resonant fast-ions (see [3] and references therein). The $n = 2$ mode also features rapid downward chirps until $t \sim 440$ ms. Afterwards, while the $n = 2$ mode is persistent, it nonetheless features noticeable variations in frequency and amplitude on times scale of ∼1 ms. This type of persistence is also sometimes observed and is another possible result of interaction with the resonant fast-ions (see [3] and references therein).

The modes in figure 7 are also identified as TAEs based on their frequencies and toroidal mode numbers, which agree with expectations for TAEs. A TAE with a toroidal mode number of n and a pair of dominant poloidal harmonics with mode numbers m and $m + 1$ will have a frequency in the TAE frequency gap, which is centered at $f_{TAE} = nf_A/(2m + 1)$ [$f_A = V_A/2\pi R$ is the Alfvén frequency at the location where $q = (m + 1/2)/n$] [24]. Equilibrium reconstruction using EFIT [58, 59] constrained by external magnetics shows that the minimum q in the plasma is ∼1.2, which is greater than 1. Since both the $q = m/n$ and $q = (m + 1)/n$ rational surfaces must exist in the plasma for a TAE to exist, the minimum m for the $n = 2$, 3 and 4 modes (corresponding to the highest possible value of f_{TAE}) would be $m = 3$, 4 and 5. Using f_{A0} at the magnetic axis, $f_{A0} = V_{A0}/2\pi R_0 \approx 174$ kHz, the associated gap frequencies are estimated to be $f_{TAE} = 50$, 58 and 63 kHz. The modes in figure 7 propagate in the beam injection direction, so their frequencies in the lab frame are increased by a Doppler shift due to toroidal rotation. CHERS measurements indicate that the toroidal rotation frequency is $f_{ROT0} \approx 40$ kHz (in the beam injection direction) at the magnetic axis, falling to 32 kHz at $R = 1.15$, 16 kHz at $R = 1.30$ m and 0 kHz at the plasma edge. The rational surfaces where $q = (m + 1/2)/n$ for $(m, n) = (3, 2)$, (4,3) and (5,4) are located at $R = 1.26$, 1.3 and 1.34 m and the rotation is $f_{ROT} \sim 20$, 16 and 12 kHz, respectively. Assuming the Doppler shifts for the $n = 2$, 3 and 4 modes are determined by the rotation at these rational surfaces, they are ∼40, 48 and 48 kHz. This gives plasma frame frequencies of $f \sim 37$, 49 and 73 kHz, which are reasonably close to the associated TAE gap frequencies.

The measurements of mode phase in figure 7(*e*) show a strong ($\sim\pi/2$) radial variation for $R >\sim 1.3$ m that offers an insight into the physics of the modes. The plasma was up–down symmetric (to within the limits achievable by the control system), so radial phase variation in the midplane would indicate radial propagation of the mode. In particular, the observed increasing phase with radius would indicate inward propagation using the sign convention

for phase in figure 7(*e*). In ideal MHD theory, TAEs are radial standing waves, so phase would be constant in the midplane (except for 180° phase changes due to sign changes) in an up–down symmetric plasma [23, 24]. (Note that this is in the absence of plasma toroidal rotation. It is not clear from existing ideal MHD theory whether toroidal rotation changes this expectation.) Consequently, the observation of radial phase variation in the midplane would clearly indicate that non-ideal MHD physics plays an important role in the mode dynamics. These measurements were made approximately in the midplane of the plasma. One possible non-ideal effect that might explain the phase variation is offered by a recent comparison of reverse shear Alfvén eigenmode (RSAE) structure measurements in the DIII-D tokamak with predictions from the TAE/FL code [46, 47]. The measurements show a radial phase variation in the midplane. RSAEs are similar in many respects to TAEs [23], including frequency and wavenumber, and they often couple TAEs [60]. They are also predicted to be radial standing waves in ideal MHD theory [22, 23]. The comparison with predictions from the TAE/FL code indicates that the RSAE phase variation is explained by the coupling of the mode to the fast-ion population. This raises the possibility that a similar mechanism may be at work for the modes shown in figure 7. Future comparison with predictions from codes including non-ideal MHD effects will be necessary to shed light on this issue. It should be noted that since the reflectometers are slightly elevated slightly above the midplane, an additional effect may contribute to the observed phase variation. TAEs in ideal MHD theory can sometimes extend across a significant portion of the minor radius and have a broad spectrum of poloidal harmonics peaking at different locations [61, 62]. Specifically, for a TAE with toroidal mode number n, the harmonic with poloidal mode number m peaks where $m \approx nq(r)$ ($q(r)$ is the safety factor). Since $q(0) \sim 1$ and $q \gg 1$ at the edge for the plasmas considered here, the poloidal mode number of the dominant harmonic can vary substantially with radius. This can give rise to a substantial phase variation, since a measurement taken at a poloidal angle θ slightly above the midplane at minor radius r will have a phase shift given by $\phi(r) \sim m(r)\theta$, where $m(r)$ is the dominant poloidal harmonic at r. The contribution of this effect to the TAE phase variation can potentially be evaluated in future experiments by observing the phase variation as the plasma is moved a small distance vertically.

3.3. Tearing modes

Tearing modes and kinks are commonly observed in NSTX plasmas [6–10]. The upgraded reflectometer array offers a powerful new tool for their investigation. Figure 8 shows the first such measurements, representing the first application of reflectometry to the investigation of tearing modes in NSTX. The measurements obtained with the array offer evidence of coupling between a tearing mode and an external kink. Figure 8(*a*) shows the fluctuation spectrum (shot 138940) from an edge reflectometer (30 GHz) in which a coherent mode and its 2nd and 3rd harmonics appear at ∼9, 18 and 27 kHz. Measurements from a toroidally distributed array of edge magnetic coils indicate that the $n = 9$ kHz mode has a toroidal mode number of $n = 1$ (propagating in the direction of the plasma toroidal rotation). Figure 8(*b*) shows the displacement amplitude of the mode at the four different times marked on the spectrum in figure 8(*a*), using the bandwidths and record lengths indicated in the figure for the analysis. The ranges of the cutoff densities and locations of the reflectometer array are indicated in figure 8(*c*), which shows density profiles from times early and late in the mode lifetime (figure 8(*a*)).

The $f = 9$ kHz mode is identified as a tearing mode using observations of the density and temperature profile evolution from MPTS. The density profiles shown in figure 8(*c*), as well as the electron temperature profiles from MPTS (not shown) exhibit a significant flat region near $R \sim 1.21$ m during the lifetime of the mode, indicating the presence of a magnetic

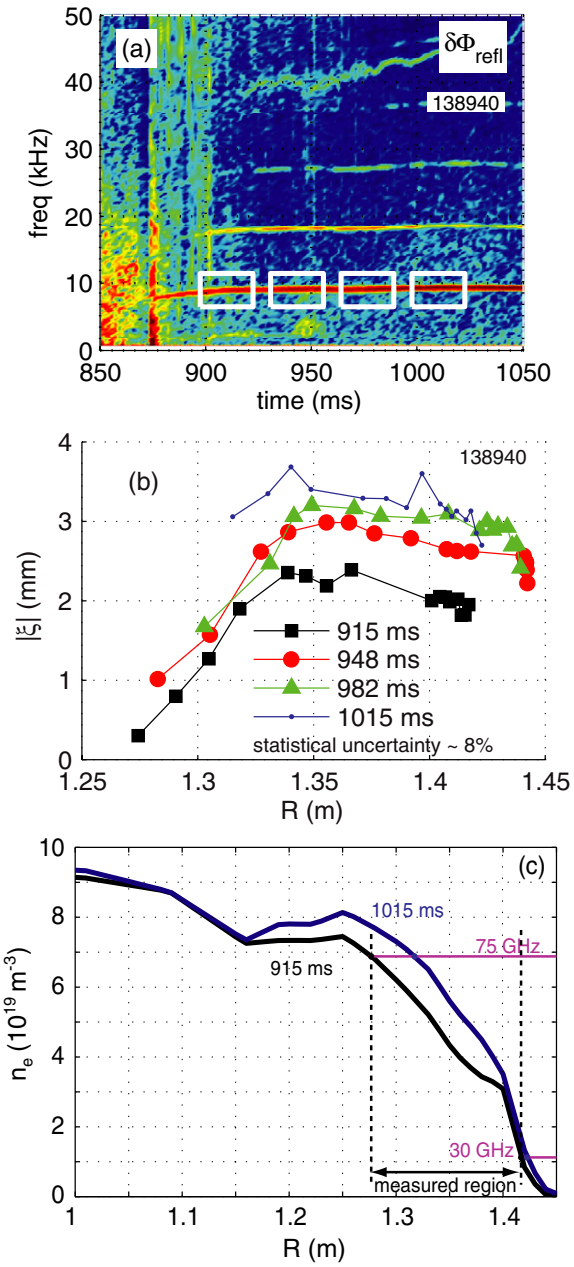

Figure 8. (*a*) Edge reflectometer (30 GHz at $R \sim 1.42$ m) spectrum showing coherent mode and its harmonics ($f \sim 9$, 18, 27 kHz); (*b*) radial structure of effective displacement amplitude of coherent mode (analysis times and bandwidths indicated by rectangles in times in figure 8(*a*)); and (*c*) MPTS measurement of density profiles with radial range and density range indicated for reflectometer array cutoffs.

island at that location. The flat region in both profiles is observed to develop during the onset of the mode between $t \sim 865$ ms and $t \sim 900$ ms, suggesting that the coherent mode is responsible for the flattening. The identification is further supported by the observation that CHERS measurements show a toroidal rotation of $f_{\mathrm{ROT}} \sim 9$ kHz in the flat region during the

lifetime of the mode. The frequency of the coherent mode is consistent with the expectation for a magnetic island at rest in the plasma frame in the flat region.

An interesting feature of the mode structure measurement in figure 8(*b*) is that, in the region accessible to the reflectometer array, it differs significantly from the expectation for a tearing mode, resembling, instead, an external kink. The effective displacement gradually approaches zero from $R \sim 1.35$ m to $R \sim 1.25$ m, which is near the edge of the flat region in the density profile. However, the flat region caused by an island results from spreading of the density contours of the plasma away from the rational surface at the poloidal location of the island. This would cause the amplitude of the displacement oscillation observed by a reflectometer to peak at the edge of the island and fall off with distance [6]. Away from the flat region in the density profile, from $R \sim 1.35$ m to the outermost measurement close to the plasma edge, effective displacement is nearly constant with radius, giving little indication of vanishing at the plasma edge. This structure indicates that the $f = 9$ kHz tearing mode is coupled to an external kink. While coupling of tearing modes to kinks has been extensively investigated in NSTX [6, 8–10] and other tokamaks [48–51], little attention has been given to the edge structure of the coupled kink-tearing modes. Notably, the peak–peak effective displacement from $R \sim 1.35$ m to the plasma edge ranges from $\sim$5 mm to $\sim$7 mm over time as the mode evolves. This is $>\sim$5% of the $\sim$8 cm width of the flat region in figure 8(*c*), which is not insignificant. These results indicate that fixed-boundary calculations, which force the edge displacement to be zero, are insufficient for understanding the evolution of coupled kink-tearing modes.

4. Summary

In summary, NSTX possesses a broad spectrum of global coherent modes that impact on plasma performance in a variety of ways. The investigation of these modes, including Alfvén eigenmodes, kink and tearing modes, is routinely facilitated in NSTX by an array of fixed-frequency quadrature reflectometers. The array has recently been significantly upgraded to 16 channels. The upgraded array consists of two eight-channel systems with frequencies—generated with the aid of NTLs—in the ranges 30–50 GHz and 55–75 GHz. This represents a significant improvement in the spatial sampling and achievable resolution of spatial structure measurements, while also allowing access to higher density, higher performance plasmas. The upgrade extends the accessible equilibrium density range to $n_{\mathrm{cutoff}} = (1.1\text{–}6.9) \times 10^{19}\ \mathrm{m}^{-3}$. This affords access to the core of high-power (6 MW) beam-heated H-mode plasmas, where the typical pedestal (i.e. edge) density is $\sim 5 \times 10^{19}\ \mathrm{m}^{-3}$.

The extended capabilities of the array have been exploited to reveal new physics related to several types of global modes. Structure measurements of CAEs and GAEs have been obtained for the first time in the core of an NSTX high-power beam-heated H-mode plasma. Previously reported correlation of GAEs activity with enhanced electron thermal transport in the core of such plasmas has motivated an investigation of the role of GAEs in the transport. The CAE structures reported here are very strongly core-localized, contrary to expectations, suggesting they may also be a candidate for explaining the enhanced transport for reasons similar to those hypothesized for GAEs. This work motivates theoretical analysis of the CAE to understand their potential contribution to core transport. TAE structure measurements have been obtained with significantly improved spatial sampling. Measurements of TAE phase, the first such in NSTX, show strong radial variation indicating inward propagation caused by non-ideal MHD effects. Tearing mode structure measurements show unambiguous evidence of coupling to an external kink. This highlights the importance of edge structure and boundary conditions in the future investigation of coupled-kink tearing modes, a topic of active investigation in NSTX

and other tokamaks. All these structure measurements represent significant advances in the investigation and understanding of global modes in NSTX and motivate future experiments and theoretical analysis.

Acknowledgment

This work was supported by US DOE Grant Nos DE-FG02-99ER54527 and DE-AC02-09CH11466.

References

[1] Hender T C *et al* 2007 *Nucl. Fusion* **47** S128
[2] Fasoli A *et al* 2007 *Nucl. Fusion* **47** S264
[3] Heidbrink W W 2008 *Phys. Plasmas* **15** 055501
[4] Stutman D, Delgado-Aparicio L, Gorelenkov N, Finkenthal M, Fredrickson E, Kaye S, Mazzucato E and Tritz K 2009 *Phys. Rev. Lett.* **102** 115002
[5] Ono M *et al* 2000 *Nucl. Fusion* **40** 557
[6] Menard J E *et al* 2005 *Nucl. Fusion* **45** 539
[7] Menard J E *et al* 2006 *Phys. Rev. Lett.* **97** 095002
[8] Gerhardt S P *et al* 2009 *Nucl. Fusion* **49** 032003
[9] Breslau J, Chance M S, Chen J, Fu G, Gerhardt S, Gorelenkov N, Jardin S C and Manickam J 2011 *Proc. 23rd IAEA Fusion Energy Conf. (Daejon, Republic Of Korea, 11–16 October 2010)* THS/P2-03 http://www-pub.iaea.org/mtcd/meetings/PDFplus/2010/cn180/cn180_papers/ths_p2-03.pdf
[10] Gerhardt S P *et al* 2011 *Nucl. Fusion* **51** 033004
[11] Fredrickson E D, Gorelenkov N, Cheng C Z, Bell R, Darrow D, Johnson D, Kaye S, LeBlanc B and Menard J 2001 *Phys. Rev. Lett.* **87** 145001
[12] Gorelenkov N N, Fredrickson E, Belova E, Cheng C Z, Gates D, Kaye S and White R 2003 *Nucl. Fusion* **43** 228
[13] Fredrickson E D, Chen L and White R 2003 *Nucl. Fusion* **43** 1258
[14] Fredrickson E D *et al* 2006 *Phys. Plasmas* **13** 056109
[15] Fredrickson E D *et al* 2007 *Phys. Plasmas* **14** 102510
[16] Gorelenkov N N, Berk H L, Fredrickson E, Sharapov S E and JET EFDA Contributors 2007 *Phys. Lett.* A **370** 70
[17] Gorelenkov N N *et al* 2009 *Phys. Plasmas* **16** 056107
[18] Eremin D Yu and Könies A 2010 *Phys. Plasmas* **17** 012108
[19] McGuire K M *et al* 1983 *Phys. Rev. Lett.* **50** 891
[20] White R B, Goldston R J, McGuire K, Allen Boozer H, Monticello D A and Park W 1983 *Phys. Fluids* **26** 2958
[21] Chen L, White R B and Rosenbluth M N 1984 *Phys. Rev. Lett.* **52** 1122
[22] Berk H L, Borba D N, Breizman B N, Pinches S D and Sharapov S E 2001 *Phys. Rev. Lett.* **87** 185002
[23] Breizman B N, Berk H L, Pekker M S, Pinches S D and Sharapov S E 2003 *Phys. Plasmas* **10** 3649
[24] Cheng C Z and Chance M S 1986 *Phys. Fluids* **29** 3695
[25] Wong K L *et al* 1991 *Phys. Rev. Lett.* **66** 1874
[26] Heidbrink W W, Strait E J, Doyle E, Sager G and Snider R T 1991 *Nucl. Fusion* **31** 1635
[27] Appert K, Gruber R, Troyon F and Vaclavik J 1982 *Plasma. Phys.* **24** 1147
[28] Weller A, Spong D A, Jaenicke R, Lazaros A, Penningsfeld F P and Sattler S 1994 *Phys. Rev. Lett.* **72** 1220
[29] Mahajan S M and Ross D W 1983 *Phys. Fluids* **26** 2561
[30] Coppi B, Cowley S, Kulsrud R, Detragiache P and Pegoraro F 1986 *Phys. Fluids* **29** 4060
[31] Gorelenkov N N and Cheng C Z 1995 *Nucl. Fusion* **35** 1743
[32] McClements K G, Gryaznevich M P, Sharapov S E, Akers R J, Appel L C, Counsell G F, Roach C M and Majeski R 1999 *Plasma Phys. Control. Fusion* **41** 661
[33] Bell R E and Feder R 2010 *Rev. Sci. Instrum.* **81** 10D724
[34] Fredrickson E D, Gorelenkov N N, Bell R E, Menard J E, Roquemore A L, Kubota S, Crocker N A and Peebles W 2006 *Nucl. Fusion* **46** S926
[35] Gorelenkov N N, Fredrickson E D, Heidbrink W W, Crocker N A, Kubota S and Peebles W A 2006 *Nucl. Fusion* **46** S933
[36] Crocker N A *et al* 2008 *Phys. Plasmas* **15** 102502
[37] Podestà M *et al* 2009 *Phys. Plasmas* **16** 056104
[38] Fredrickson E D *et al* 2009 *Phys. Plasmas* **16** 122505

[39] Podestà M, Bell R E, Fredrickson E D, Gorelenkov N N, LeBlanc B P, Heidbrink W W, Crocker N A, Kubota S and Yuh H 2010 *Phys. Plasmas* **17** 122501
[40] Fredrickson E D *et al* 2011 *Proc. 23rd IAEA Fusion Energy Conf. (Daejon, Republic of Korea,, 11–16 October 2010)* EXW/P7-06 http://www-pub.iaea.org/MTCD/Meetings/PDFplus/2010/cn180/cn180_papers/exw_P7-06.pdf
[41] Peebles W A, Rhodes T L, Hillesheim J C, Zeng L and Wannberg C 2010 *Rev. Sci. Instrum.* **81** 10D902
[42] Kolesnichenko Y I, Yakovenko Y V and Lutsenko V V 2010 *Phys. Rev. Lett.* **104** 075001
[43] Gorelenkov N N, Stutman D, Tritz K, Boozer A, Delgado-Aparicio L, Fredrickson E, Kaye S and White R 2010 *Nucl. Fusion* **50** 084012
[44] Tritz K *Bull. Am. Phys. Soc.* **55** BAPS.2010.DPP.PI2.2 http://Meetings.aps.org/link/BAPS.2010.DPP.PI2.2
Tritz K *et al* 2011 *Phys. Plasmas* in preparation
[45] Classen I G J *et al* 2010 *Rev. Sci. Instrum.* **81** 10D929
[46] Greenfield C M 2011 *Proc. 23rd IAEA Fusion Energy Conf. (Daejon, Republic Of Korea, 11–16 October 2010* OV/1-4 http://www-pub.iaea.org/MTCD/Meetings/PDFplus/2010/cn180/cn180_papers/ov_1-4.pdf
[47] Tobias B J, Classen I G J, Domier C W, Heidbrink W W, Luhmann N C Jr, Nazikian R, Park H K, Spong D A and Van Zeeland M A 2011 *Phys. Rev. Lett.* **106** 075003
[48] Gude A, Günter S, Sesnic S and the ASDEX Upgrade Team 1999 *Nucl. Fusion* **39** 127
[49] Fredrickson E D 2002 *Phys. Plasmas* **9** 548
[50] Nave M F F, Lazzaro E, Coelho R, Belo P, Borba D, Buttery R J, Nowak S, Serra F and EFDA-JET Contributors 2003 *Nucl. Fusion* **43** 179
[51] Brennan D J, Turnbull A D, Chu M S, LaHaye R J, Lao L L, Osborne T H and Galkin S A 2007 *Phys. Plasmas* **14** 056108
[52] Nazikian R, Kramer G J and Valeo E 2001 *Phys. Plasmas* **8** 1840
[53] LeBlanc B P, Bell R E, Johnson D W, Hoffman D E, Long D C and Palladino R W 2003 *Rev. Sci. Instrum.* **74** 1659
[54] Levinton F M and Yuh H 2008 *Rev. Sci. Instrum.* **79** 10F522
[55] Lee K C, Domier C W, Johnson M, Luhmann N C and Park H 2004 *Rev. Sci. Instrum.* **75** 3433
[56] Levinton F M *et al* 2007 *Phys. Plasmas* **14** 056119
[57] http://w3.pppl.gov/~jmenard/software/lrdfit/lrdfit-index.htm
[58] Sabbagh S A *et al* 2001 *Nucl. Fusion* **41** 1601
[59] Lao L L, St. John H, Stambaugh R D, Kellman A G and Pfeiffer W 1985 *Nucl. Fusion* **25** 1611
[60] Van Zeeland M A , Austin M E, Gorelenkov N N, Heidbrink W W, Kramer G J, Makowski M A, Mckee G R, Nazikian R, Ruskov E and Turnbull A D 2007 *Phys. Plasmas* **14** 056102
[61] Cheng C Z 1991 *Phys. Fluids* B **3** 2463
[62] Fu G Y, Cheng C Z, Budny R, Chang Z, Darrow D S, Fredrickson E, Mazzucato E, Nazikian R, Wong K L and Zweben S 1996 *Phys. Plasmas* **3** 4036